





Efficient Mott insulator-metal transition by an intense terahertz electric field pulse via quantum tunneling

N. Takamura ¹, T. Miyamoto ^{1,*}, S. Liang,¹ K. Asada,¹ T. Terashige,² Y. Takahashi,³
T. Hasegawa ⁴ and H. Okamoto ^{1,2,†}

¹*Department of Advanced Materials Science, University of Tokyo, Kashiwa, Chiba 277-8561, Japan*

²*AIST-UTokyo Advanced Operand-Measurement Technology Open Innovation Laboratory (OPERANDO-OIL), National Institute of Advanced Industrial Science and Technology (AIST), Kashiwa, Chiba 277-8589, Japan*

³*Department of Chemistry, Faculty of Science and Graduate School of Chemical Sciences and Engineering, Hokkaido University, Sapporo, Hokkaido 060-0810, Japan*

⁴*Department of Applied Physics, University of Tokyo, Bunkyo-ku, Tokyo 113-8656, Japan*



(Received 4 November 2022; revised 1 February 2023; accepted 3 February 2023; published 27 February 2023)

When a semiconductor is subjected to a strong electric field, carriers are generated via quantum tunneling; this is termed as dielectric breakdown. Thus, using a terahertz pulse to drive the dielectric breakdown in Mott insulators, which exhibit variations in their electronic structures under carrier doping, a filling-controlled transition can be induced in the subpicosecond time scale. However, to generate carriers via quantum tunneling in a material with a band gap in the visible or near-infrared regions, an electric field pulse significantly exceeding 1 MV cm^{-1} is necessary. In this paper, using an organic molecular compound, bis(ethylenedithio)tetrathiafulvalene-difluorotetracyanoquinodimethane, which is a typical one-dimensional (1D) Mott insulator with a Mott gap of 0.7 eV, we aimed at realizing carrier generation and metallization via a strong electric field component of a terahertz pulse enhanced with an organic nonlinear optical crystal up to 2.8 MV cm^{-1} . Even after the terahertz electric field decays, the reflectivity change caused by the terahertz pulse remains; this is different from the case involving the use of weaker electric fields. More importantly, this response indicates a threshold behavior against the electric field amplitude, which is characteristic of carrier generation via the quantum tunneling process. Furthermore, transient reflectivity spectra across the mid-infrared region could be reproduced well by numerical simulations using the Drude model, in which inhomogeneous carrier distributions are considered. The observed Drude response of the doublons and holons was ascribed to the spin-charge separation characteristic of 1D strongly correlated electron systems. We also demonstrate that the energy efficiency of such carrier generation by the terahertz pulse excitation is at least five times greater than that when using photoexcitation beyond the Mott gap. This indicates that excitation with the strong terahertz pulse is more effective for carrier doping in solids; thus, the proposed method is expected to be widely applicable for the electronic-state control of various correlated electron materials in which chemical carrier doping is currently difficult.

DOI: [10.1103/PhysRevB.107.085147](https://doi.org/10.1103/PhysRevB.107.085147)

I. INTRODUCTION

When a Mott insulator is doped with carriers, its electronic structure can change significantly; for instance, certain doped Mott insulators become metallic [1]. A typical example is the carrier doping of the parent compounds of high- T_c cuprates with substitutions of constituent ions, which causes metallization and superconductivity at low temperatures [2,3]. Such filling-controlled Mott transitions have long been studied as a central issue in the physics of strongly correlated electron systems. Another effective method for carrier doping in solids is photoexcitation. When a Mott insulator is excited by a laser pulse with a photon energy exceeding the Mott gap, a Mott insulator-to-metal transition can occur; this is termed as a photoinduced Mott transition. Previous studies using femtosecond pump-probe

spectroscopy have revealed that such a phenomenon is observed in various Mott insulators; the bromine-bridged nickel-chain compound of $[\text{Ni}(\text{chxn})_2\text{Br}]\text{Br}_2$ (chxn = cyclohexanediamine) [4], the organic molecular compound of bis(ethylenedithio)tetrathiafulvalene-difluorotetracyanoquinodimethane (ET- F_2TCNQ) [5], and layered cuprates of Nd_2CuO_4 and La_2CuO_4 [6,7]. The advantage of this method is that carrier doping can be achieved without any additional structural changes, which can occasionally occur during carrier doping via the substitution of constituent elements. In addition, information regarding the dynamics of the electronic state changes can be obtained based on the time evolution of the spectral variations caused by photoexcitation. This enables investigations into the role of the electron-lattice and charge-spin interactions and electron correlations, under both the ground and photoexcited states [8–14]. However, carrier doping via photoexcitation imposes a large amount of energy on the material, which increases the temperature of the charge, spin, and lattice systems [7,10]. Such an increase in temperature is known to

*miyamoto@k.u-tokyo.ac.jp

†okamoto@k.u-tokyo.ac.jp

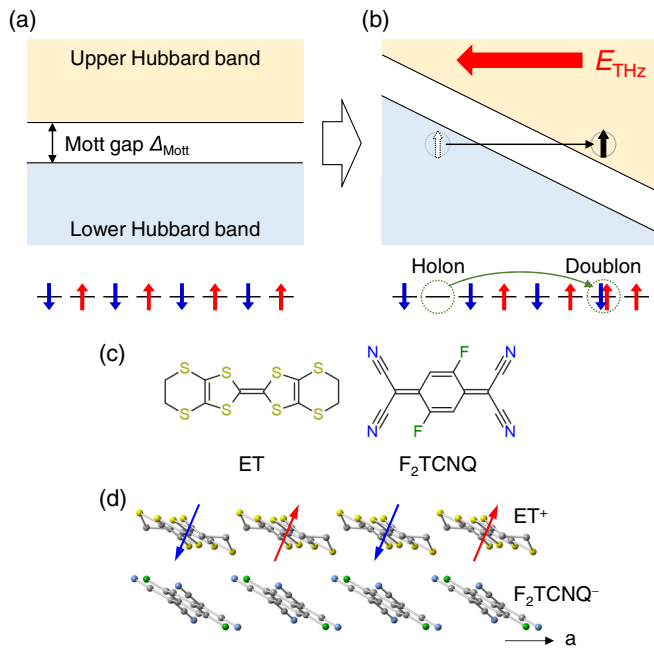


FIG. 1. Quantum tunneling process by a strong electric field in a half-filled one-dimensional Mott insulator of ET-F₂TCNQ. (a) Schematic band structure. (b) A generation of a doublon-holon pair by an electric field of a terahertz pulse E_{THz} . (c) Molecular structures of ET and F₂TCNQ. (d) Molecular arrangements along the normal to the ab plane in ET-F₂TCNQ.

occur during various photoinduced transition phenomena. It necessarily delays the recovery of the system to its original state and complicates the electronic-state changes caused by photoexcitation.

Considering these existing issues, we developed an approach for carrier doping in solids using a terahertz pulse. The recent development of the terahertz pulse generation method using the nonlinear optical crystal LiNbO₃, which is called the pulse-front tilting method, has enabled the generation of nearly monocyclic terahertz pulses with electric field amplitudes considerably exceeding 100 kV cm^{-1} [15,16]. Using such intense electromagnetic pulses, attempts have been devoted toward controlling the physical properties of solids [17], such as the magnetization and (electro)magnons [18–20], polarizations [21–24], impact ionization and carrier amplification [25,26], electrical conductivity [27], and superconducting gaps [28,29]. Regarding Mott insulators, theoretical studies have predicted that insulator-metal transitions can be induced using intense electric field pulses [30–32]. A conceptual diagram of this phenomenon is shown in Figs. 1(a) and 1(b). When a strong electric field pulse is applied to a Mott insulator, the upper and lower Hubbard bands are spatially inclined, which can lead to the generation of doublon-holon pairs through a quantum tunneling process, as shown in Fig. 1(b). Fundamentally, this is identical to the Zener tunneling phenomenon, which is well known in semiconductors [33]. Interestingly, in Mott insulators, carrier generation may trigger a change in the electronic structure, resulting in metallization.

Carrier generation and metal-insulator transition via the quantum tunneling by a mid-infrared pulse excitation has

been studied in a correlated electron system of VO₂ [34]. This compound undergoes an insulator-metal transition with a large structural change at 340 K below which the insulating state is stabilized by the strong dimerization of V ions. Therefore, VO₂ is not a pure Mott insulator but most likely carries both electronic and structural aspects in its metal-insulator transition. In the study of the mid-infrared pulse excitation on VO₂ [34], a strong mid-infrared electric field induced the quantum tunneling process of carriers, which in turn destabilizes the dimer of V ions and causes a structural change, resulting in an insulator-metal transition. As a mid-infrared pulsed excitation in Mott insulators, the study on an organic molecular compound ET-F₂TCNQ has been reported [35,36]. This compound is a half-filled one-dimensional (1D) Mott insulator with a Mott gap energy of $\sim 0.7 \text{ eV}$ [5,37] and is also a target material in this paper. In that study, it was revealed that the resonant excitation of intramolecular vibrations by mid-infrared pulses modulates the magnitude of the on-site Coulomb repulsion energy U , which gives rise to the modulation of a transition energy of the exciton corresponding to the Mott gap [35,36]. However, neither carrier generation nor field-induced metallization was observed in that study.

In a more recent study, using the organic molecular compound κ -(ET)₂Cu[N(CN)₂]Br, which is a two-dimensional (2D) Mott insulator with a significantly small Mott gap energy of $\sim 30 \text{ meV}$ on a diamond substrate at low temperatures, carrier generation via quantum tunneling caused by irradiation with a terahertz pulse featuring an electric field amplitude of 180 kV cm^{-1} was achieved; the resultant metallization was reported based on broadband transient absorption spectroscopy over the near- to mid-infrared regions [38]. However, similar phenomena caused by terahertz pulses have not been reported for Mott insulators with larger optical gaps; this is likely because these large gaps would necessitate considerably stronger electric fields. For instance, considering a 1D Mott insulator with an optical gap energy of 0.7 eV , an electric field of 3 MV cm^{-1} is predicted to be necessary for carrier generation [32].

In this paper, we aimed to achieve insulator-to-metal transition via a quantum tunneling process in a typical 1D Mott insulator ET-F₂TCNQ [Figs. 1(c) and 1(d)], with a Mott gap energy of 0.7 eV [5,37], by using a strong terahertz pump pulse with a maximum electric field of $\sim 3 \text{ MV cm}^{-1}$; this was realized using a second-order nonlinear optical crystal of 4-*N,N*-dimethylamino-4'-*N'*-methyl-stilbazolium 2,4,6-trimethylbenzenesulfonate (DSTMS) [39]. By applying terahertz pulse pump optical reflectivity probe spectroscopy to ET-F₂TCNQ, we demonstrated that the Mott insulator-to-metal transition is driven by a terahertz electric field. Detailed analyses of the spectral changes in the mid-infrared region revealed that the energy efficiency of the carrier generation under the terahertz electric field is considerably higher than that induced by photoexcitation beyond the Mott gap.

II. EXPERIMENTAL DETAILS

A. Sample preparations

Single crystals of ET-F₂TCNQ were grown by the recrystallization method [37]. All the optical measurements were

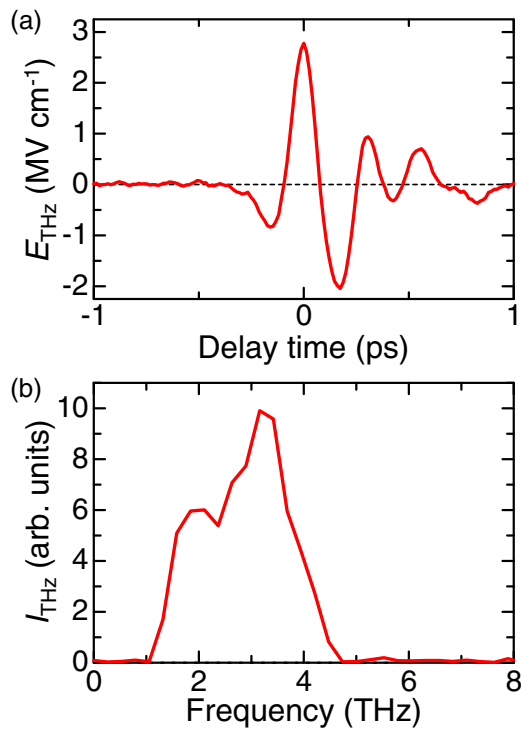


FIG. 2. (a) Electric field waveform $E_{\text{THz}}(t_d)$ and (b) Fourier power spectrum $I_{\text{THz}}(\omega)$ of the terahertz pulse.

performed on platelike single crystals with the largest ab plane. The typical a - and b -axis lengths of the single crystals were 1 and 2.5 mm, respectively. Their typical thickness is $\sim 200 \mu\text{m}$.

B. Terahertz pulse pump optical reflectivity probe measurements

For the terahertz pulse pump optical reflectivity probe measurements, the light source used was a Ti:sapphire regenerative amplifier (RA) with a repetition rate of 1 kHz, central wavelength of 800 nm, pulse width of 100 fs, and pulse energy of 7 mJ. The output was divided into two beams. One was introduced to an optical parametric amplifier (OPA), where it was converted into a 1500 nm (0.8 eV) pulse with a pulse energy of 0.8 mJ. This pulse was incident to an organic nonlinear optical crystal DSTMS. Thus, through optical rectification in the DSTMS crystal, an intense terahertz pulse was generated [40,41]. Figure 2(a) shows the typical electric field waveform $E_{\text{THz}}(t_d)$ of a terahertz pulse reconstructed by the deconvolution procedure from the waveform, measured using an electro-optic (EO) sampling with a GaP crystal [42]. The spot diameter (full width at half maximum) of the terahertz pulse on the sample surface was $135 \mu\text{m}$, and the maximum electric field amplitude was $\sim 2.8 \text{ MV cm}^{-1}$. The time origin was set at the maximum of the terahertz electric field, whereas the delay time t_d of the probe pulse relative to the terahertz pump pulse was controlled using a mechanical delay stage. Figure 2(b) shows the Fourier power spectrum of the terahertz pulse. The central frequency is $\sim 3 \text{ THz}$. Further, the second beam from the RA was introduced into another OPA to generate a probe pulse with a photon energy of 0.07–1.12 eV. All

the optical measurements were performed on the ab plane of ET-F₂TCNQ single crystals at 294 K. The electric fields of both the pump and probe pulses were parallel to the a axis.

C. Measurements of steady-state optical spectra

The polarized reflectivity spectrum of ET-F₂TCNQ along the a axis was measured on a single crystal with a thickness of $\sim 200 \mu\text{m}$, using a Fourier transform infrared spectrometer (0.025–1.2 eV) and a spectrometer with a grating monochromator (0.46–6.2 eV), both of which were equipped with an optical microscope. In the terahertz frequency region, we applied two systems of terahertz time-domain spectroscopy on a thin single crystal of ET-F₂TCNQ with a thickness of $41 \mu\text{m}$ with the transmission geometry. In the first measurement system (System 1), the transmittance in the region of 1–3 THz (0.004–0.012 eV) was measured using a terahertz pulse generated by the optical rectification method from the organic nonlinear optical crystal DSTMS, which was identical to that used in the terahertz pulse pump optical reflectivity probe measurements described in Sec. II B. The terahertz pulse from the DSTMS crystal used in this measurement was attenuated $< 100 \text{ kV cm}^{-1}$. In the second measurement system (System 2), the transmittance in the region of 3–8 THz (0.012–0.033 eV) was measured using a terahertz pulse generated by the air plasma generation method [43,44]. In this system, the light source used was a Ti:sapphire RA with a repetition rate of 1 kHz, central wavelength of 800 nm, pulse width of 25 fs, and pulse energy of 2 mJ. The output was divided into two beams. One was used for the generation of terahertz pulses via air-plasma induced terahertz radiation, and the other was used as a sampling pulse for the EO sampling of terahertz electric fields. The electric field waveform of the terahertz pulse transmitted through the thin single crystal was measured via the EO sampling with a GaP crystal in both of two types of measurements.

D. Measurements of nonlinear absorptions of terahertz pulses

For measuring the nonlinear absorptions of relatively strong terahertz pulses, we used a setup like that for the transmission measurements using the terahertz pulse from the DSTMS crystal, as mentioned in Sec. II C. To ensure linearity in the EO sampling, four Si plates were inserted into the optical path of the terahertz pulse passing through the ET-F₂TCNQ single crystal.

III. RESULTS AND DISCUSSIONS

A. Optical absorption spectrum of ET-F₂TCNQ

ET-F₂TCNQ is a quasi-1D organic molecular compound. The molecular structures of ET and F₂TCNQ are presented in Fig. 1(c) [37]. An electron was transferred from the donor molecule of ET to the acceptor molecule of F₂TCNQ. The F₂TCNQ⁻ molecules are almost isolated, whereas the ET molecules are stacked along the a axis, forming a half-filled 1D electronic system, as shown in Fig. 1(d). Owing to the strong on-site Coulomb repulsion U , which overcomes the transfer energy t between neighboring ET molecules,

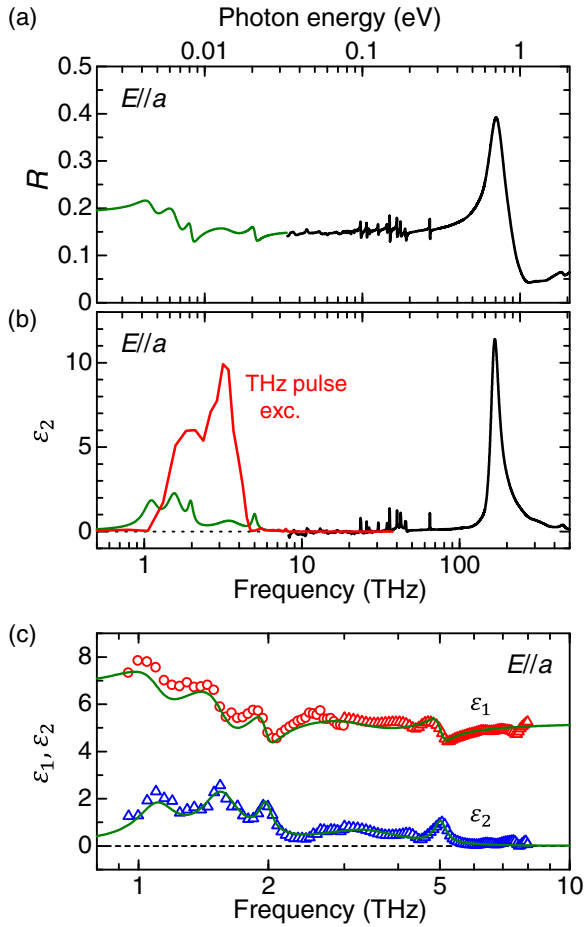


FIG. 3. Steady-state optical spectra on ET-F₂TCNQ. (a) The polarized reflectivity (R) spectrum (the black line) measured with the electric field of lights E parallel to the a axis ($E\parallel a$). (b) The ϵ_2 spectrum with $E\parallel a$. The spectrum >8 THz (the solid line) was obtained from the Kramers-Kronig (KK) transformation of the R spectrum in (a). The red line shows the Fourier power spectrum of the terahertz pump pulse, which is the same as that shown in Fig. 2(b). (c) The spectra of ϵ_1 (open circles) and ϵ_2 (open triangles) in the terahertz region obtained by the terahertz time-domain spectroscopy. The green lines in (b) and (c) are the fitting curves for the ϵ_1 and ϵ_2 spectra in the terahertz region assuming the Lorentz oscillators, the parameters of which were shown in Table I. The green line in (a) is the calculated R spectrum obtained from the ϵ_1 and ϵ_2 spectra (the green lines) in (c).

electrons are localized at each site, and this compound is a half-filled 1D Mott insulator [45,46].

The black line in Fig. 3(a) shows the polarized reflectivity spectrum $R(\omega)$, with the electric field of light parallel to the a axis. The spectrum of the imaginary part of the dielectric constant $\epsilon_2(\omega)$, shown by the black line in Fig. 3(b), was obtained using the Kramers-Kronig (KK) transformation of the $R(\omega)$ spectrum. In the $\epsilon_2(\omega)$ spectrum, a sharp peak corresponding to the transition beyond the Mott gap appears at 0.694 eV. Strictly, this peak is ascribed to an exciton consisting of a bound pair of a doublon and holon [45,46]. Figure 3(c) shows the real part ϵ_1 and imaginary part ϵ_2 of the complex dielectric constant $\tilde{\epsilon}(\omega) = \epsilon_1 + i\epsilon_2$ in the terahertz region. Several small

TABLE I. The fitting parameters of the Lorentz oscillators for the calculation of complex dielectric constant ($\tilde{\epsilon}$) and reflectivity (R) spectra in the terahertz region shown by green solid lines in Figs. 3(a)–3(c).

| i | f_i | $\omega_i/2\pi$ (THz) | $\gamma_i/2\pi$ (THz) |
|-----|-------|-----------------------|-----------------------|
| 1 | 0.364 | 1.11 | 0.28 |
| 2 | 0.521 | 1.56 | 0.41 |
| 3 | 0.117 | 1.97 | 0.18 |
| 4 | 0.261 | 3.53 | 1.55 |
| 5 | 0.071 | 5.01 | 0.39 |

structures are observed in both the ϵ_1 and ϵ_2 spectra, which are ascribed to phonon absorption. These spectra were analyzed assuming the Lorentz oscillators. When several Lorentz oscillators exist, $\tilde{\epsilon}(\omega)$ can be expressed as follows:

$$\tilde{\epsilon}(\omega) = \epsilon_\infty + \sum_i \frac{f_i \omega_i^2}{\omega_i^2 - \omega^2 - i\gamma_i \omega}, \quad (1)$$

where ω_i , γ_i , and f_i are the frequency, damping constant, and oscillator strength of oscillator i , respectively. Here, ϵ_∞ is the dielectric constant at high frequencies. For ϵ_∞ , we used a value of ~ 5.16 , obtained from the reflectivity at 0.04–0.07 eV, where the absorption is negligibly small. The fitting parameters were ω_i , γ_i , and f_i . Assuming five oscillators ($i = 1-5$), the ϵ_1 and ϵ_2 spectra were almost reproduced, as shown by the green line in Fig. 3(c). The parameter values are listed in Table I. The fitting curve of the ϵ_2 spectrum was shown by the green line in Fig. 3(b). Employing the parameters in Table I, we calculated the steady-state reflectivity spectrum $R(\omega)$, which was used to extrapolate the $R(\omega)$ values below the lower energy bound of the measured region. The calculated $R(\omega)$ spectrum in the terahertz region is also depicted by the green line in Fig. 3(a).

B. Time characteristics and spectra of electric-field-induced reflectivity changes

To investigate the electric-field-induced Mott insulator-to-metal transition, we adopted terahertz pulse pump optical reflectivity probe spectroscopy. Figure 4(b) shows a typical electric field waveform $E_{\text{THz}}(t_d)$ of a terahertz pulse, where the time origin is set at the maximum electric field amplitude of the terahertz pulse. The maximum electric field value, that is, $E_{\text{THz}}(0)$, is ~ 2.8 MV cm⁻¹. The red line in Fig. 3(b) denotes the Fourier power spectrum of the terahertz pulse $I_{\text{THz}}(\omega)$. The central photon energy (frequency) is ~ 12 meV (3 THz). In the $\epsilon_2(\omega)$ spectrum in the same figure, absorptions due to phonons exist in the range of 3 meV (0.7 THz) to 25 meV (6 THz); however, they are very weak. Namely, ET-F₂TCNQ is fundamentally transparent to terahertz pulses, thus enabling us to investigate the pure electric field effects on the 1D Mott insulator state. The photon energy of the probe pulse was varied from 1.12 to 0.07 eV, and the electric fields of both the pump and probe pulses were parallel to the 1D molecular stacking axis, that is, the a axis.

First, we focused on the responses around the lowest electronic transition peak at ~ 0.7 eV. Figure 4(c) shows the time

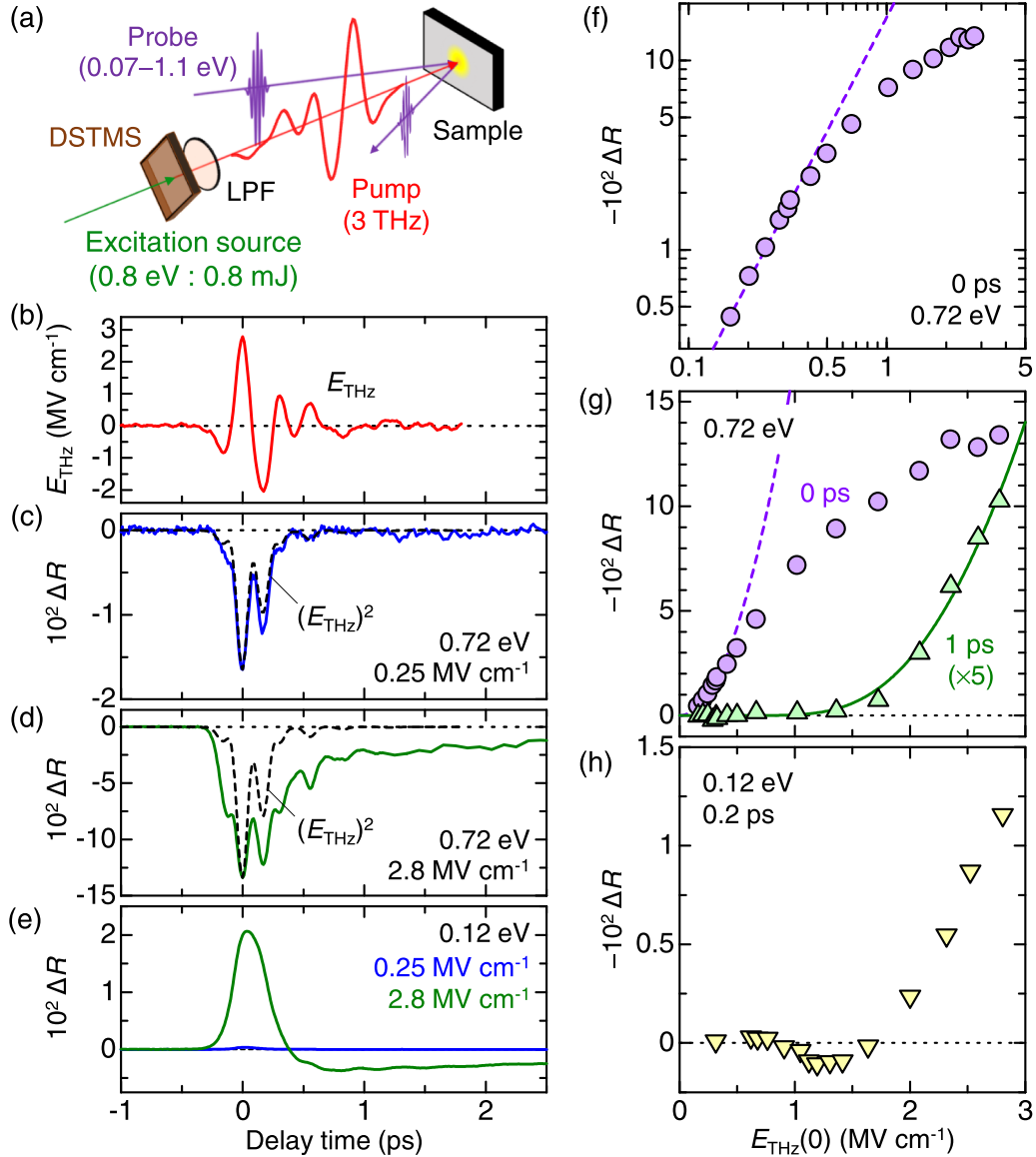


FIG. 4. Terahertz pulse pump-optical reflectivity probe spectroscopy on ET-F₂TCNQ. (a) A schematic configuration of the pump-probe measurements. (b) Electric field waveform $E_{\text{THz}}(t_d)$ of the terahertz pump pulse [the same as that shown in Fig. 2(a)]. (c) Time characteristic of reflectivity change $\Delta R(t_d)$ at 0.72 eV by the terahertz pulse with $E_{\text{THz}}(0) = 0.25 \text{ MV cm}^{-1}$. (d) Time characteristic of $\Delta R(t_d)$ at 0.72 eV by the terahertz pulse with $E_{\text{THz}}(0) = 2.8 \text{ MV cm}^{-1}$. (e) Time characteristics of $\Delta R(t_d)$ at 0.12 eV by the terahertz pulse with $E_{\text{THz}}(0) = 0.25 \text{ MV cm}^{-1}$ and 2.8 MV cm^{-1} . (f) $E_{\text{THz}}(0)$ dependence of $\Delta R(0)$ at 0.72 eV. (g) $E_{\text{THz}}(0)$ dependence of $\Delta R(0)$ and ΔR at 1 ps at 0.72 eV. The broken lines in (f) and (g) show the relation $\Delta R(0) \propto [E_{\text{THz}}(0)]^2$. The green solid line shows the fitting curve (see the text). (h) $E_{\text{THz}}(0)$ dependence of ΔR at 0.2 ps at 0.12 eV.

evolution of the reflectivity change $\Delta R(t_d)$ at 0.72 eV as a function of the delay time t_d . The electric field amplitude $E_{\text{THz}}(0)$ was 0.25 MV cm^{-1} . As can be seen, $\Delta R(t_d)$ almost follows the convolution of the square of the electric field waveform $[E_{\text{THz}}(t_d)]^2$ with the intensity profile of the probe pulse, indicated by the broken line in the same figure. These results suggest that the observed reflectivity change $\Delta R(t_d)$ in Fig. 4(c) can be attributed to a third-order optical nonlinearity described by $P^{(3)}(\omega) \propto E_{\text{THz}}(\omega \sim 0)E_{\text{THz}}(\omega \sim 0)E(\omega)$ [47], where $P^{(3)}(\omega)$ is the third-order nonlinear polarization, $E_{\text{THz}}(\omega \sim 0)$ is the terahertz electric field, and $E(\omega)$ is the electric field of the probe light. This type of nonlinear optical response in the terahertz pulse pump optical reflectivity probe

spectroscopy was previously reported for ET-F₂TCNQ [45], the 1D Mott insulator of a bromine-bridged nickel-chain compound $[\text{Ni}(\text{chxn})_2\text{Br}]\text{Br}_2$ [48], and the 2D Mott insulators of layered cuprates Nd_2CuO_4 , La_2CuO_4 , and $\text{Sr}_2\text{CuO}_2\text{Cl}_2$ [49]. The spectral feature of this component is discussed later.

Figure 4(d) shows the time evolution of $\Delta R(t_d)$ for a strong terahertz pulse with $E_{\text{THz}}(0) = 2.8 \text{ MV cm}^{-1}$. As can be seen, it does not follow the convolution of the square of the electric field waveform $[E_{\text{THz}}(t_d)]^2$ with the intensity profile of the probe pulse, indicated by the broken line. A finite negative reflectivity change remains after $t_d = 1 \text{ ps}$ when the terahertz field diminishes. This signal appears around the time origin. Furthermore, we indicate the magnitudes of $-\Delta R(t_d)$

at $t_d = 0$ ps, $-\Delta R(0)$, as a function of $E_{\text{THz}}(0)$ in Figs. 4(f) and 4(g), the horizontal axes of which have logarithmic and linear scales, respectively. The $-\Delta R(0)$ signals are proportional to the square of the electric field amplitudes $[E_{\text{THz}}(0)]^2$ below $E_{\text{THz}}(0) = 0.4$ MV cm $^{-1}$, as shown by the broken lines in Figs. 4(f) and 4(g), thereby reflecting the third-order nonlinear optical responses; however, it deviates from $[E_{\text{THz}}(0)]^2$ for $E_{\text{THz}}(0) > 0.4$ MV cm $^{-1}$ and tends to saturate around $E_{\text{THz}}(0) \sim 2$ MV cm $^{-1}$. At $t_d = 1$ ps, when the terahertz electric field disappears, the $E_{\text{THz}}(0)$ dependence of the reflectivity change $-\Delta R(1$ ps) exhibits a threshold behavior, as shown by the green triangles in Fig. 4(g). Here, $-\Delta R(1$ ps) barely appears < 1.5 MV cm $^{-1}$ but exhibits a sharp increase at stronger electric fields. The probe energy (0.72 eV) is considerably close to the peak energy of absorption (0.694 eV); therefore, the decrease in reflectivity at this energy represents a bleaching signal and possibly reflects the number of generated carriers (doublons and holons).

In inorganic semiconductors, an impact ionization is known as one of the mechanisms of electric-field-induced carrier generations [25,50]. In this process, a small number of carriers, which are originally present but localized in the system, are accelerated by an external electric field to gain energy, and the energy is used to generate carriers. The repetition of this carrier generation process causes carrier multiplication which is highly nonlinear against the electric field. As shown in Fig. 3(a), no absorption due to electronic transitions appears below the Mott gap, showing that no carriers exist in ET-F $_2$ TCNQ. Therefore, it is reasonable to consider that no carrier generation via the impact ionization mechanism occurs.

The observed threshold behavior of $-\Delta R(1$ ps) is reminiscent of the carrier generation caused by the quantum tunneling process. In 1D Mott insulators, the probability of carrier generation via quantum tunneling is proportional to $E_{\text{THz}}(0) \exp[-\pi E_{\text{th}}/E_{\text{THz}}(0)]$, where E_{th} is the threshold electric field [32]. The $[-\Delta R(1$ ps)] values at 0.72 eV are well reproduced by this exponential formula with $E_{\text{th}} = 2.37$ MV cm $^{-1}$, as shown by the solid green line in Fig. 4(g). Here, E_{th} is expressed as $E_{\text{th}} = \Delta_{\text{Mott}}/(2e\xi)$, where Δ_{Mott} is the Mott gap energy, e is the elementary charge, and ξ is the correlation length, which represents the average distance between a doublon and a holon existing in the ground state due to quantum fluctuations [32]. Using $E_{\text{th}} = 2.37$ MV cm $^{-1}$ and $\Delta_{\text{Mott}} = 0.694$ eV, ξ was estimated to be 14.7 Å. Because the distance between neighboring ET molecules along the a axis is ~ 5.8 Å, $\xi = 14.7$ Å corresponds to a distance of 2.5 sites. This estimation is detailed later in Sec. III C.

Next, we focus on the probe energy dependence of the changes in the transient reflectivity caused by the terahertz pulse. Figure 5(a) shows the $\Delta R(t_d)$ spectra at $t_d = 0, 0.3,$ and 1 ps for a relatively weak terahertz pulse with $E_{\text{THz}}(0) = 0.25$ MV cm $^{-1}$. The $\Delta R(0)$ spectrum shows a plus-minus-plus structure around the original reflectivity peak at 0.7 eV. At $t_d = 1$ ps, when the terahertz electric field diminishes, no $\Delta R(t_d)$ signals are detected. This suggests that the observed reflectivity changes around the time origin are due to the coherent nonlinear optical response, which occurs only when the terahertz electric field is applied. According to previous studies, a plus-minus-plus structure, as seen in the

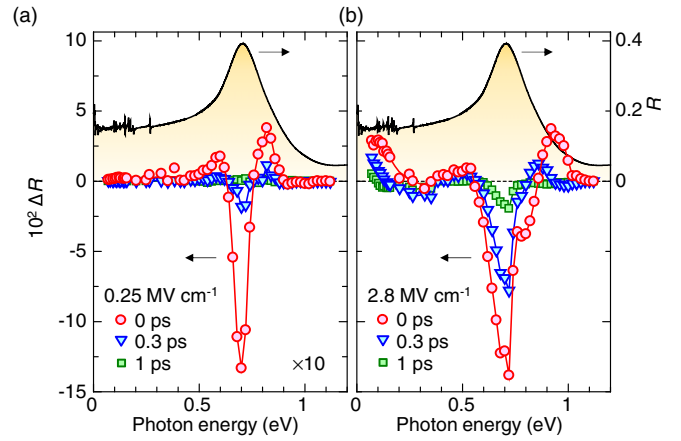


FIG. 5. Spectra of transient reflectivity changes. $\Delta R(t_d)$ spectra at $t_d = 0, 0.3,$ and 1.0 ps by the terahertz pulse with (a) $E_{\text{THz}}(0) = 0.25$ MV cm $^{-1}$ and (b) $E_{\text{THz}}(0) = 2.8$ MV cm $^{-1}$. The black solid lines show the original reflectivity (R) spectra.

$\Delta R(0)$ spectrum, commonly appears in the electroreflectance spectra of 1D Mott insulators and is ascribed to the third-order optical nonlinearity [45,48,51–53], as mentioned above. Assuming the three levels of the ground state $|0\rangle$, the one-photon-allowed excitonic state $|1\rangle$ with odd parity, and the one-photon-forbidden excitonic state $|2\rangle$ with even parity, the plus-minus-plus structure can be well reproduced; this is qualitatively explained by the sum of the low-energy shift of the excitonic state $|1\rangle$ and the induced absorption of the excitonic state $|2\rangle$, owing to the hybridization of those two states by the electric field [45,48,51–53]. These interpretations are consistent with the quadratic dependence of $[-\Delta R(0)]$ on $E_{\text{THz}}(0)$, as shown in Figs. 4(c), 4(f), and 4(g). Furthermore, in the mid-infrared region < 0.4 eV, no significant reflectivity changes were observed.

Figure 5(b) shows the $\Delta R(t_d)$ spectra of a strong terahertz pulse with $E_{\text{THz}}(0) = 2.8$ MV cm $^{-1}$. As can be seen, the spectrum of $\Delta R(t_d)$ at $t_d = 0$ ps, $\Delta R(0)$, still includes the plus-minus-plus structure due to the third-order nonlinear optical response. However, in contrast to the response to the relatively low electric field of $E_{\text{THz}}(0) = 0.25$ MV cm $^{-1}$, the negative components of $\Delta R(0)$ were relatively large as compared with the positive components around the original absorption peak. Furthermore, a finite reflectivity decrease was observed in the spectrum near the original peak at $t_d = 1$ ps after the terahertz electric field diminished; this can be ascribed to the bleaching signal due to carriers generated by the electric field via the quantum tunneling process. Carrier generation was more directly reflected by the change in reflectivity in the mid-infrared region. As shown in Fig. 5(b), the $\Delta R(t_d)$ signals monotonically increase with a decrease in the probe energy at each delay time. Thus, it was concluded that the carriers generated by the electric field would act as mobile carriers.

Figure 6(a) shows the expanded $\Delta R(t_d)$ spectra below ~ 0.4 eV for $E_{\text{THz}}(0) = 2.8$ MV cm $^{-1}$ at the three delay times of 0, 0.3, and 1 ps. In these spectra, the point where $\Delta R(t_d)$ crosses zero moves toward the lower-energy side over time. These behaviours are characteristic of the Drude response, which can be explained as follows. In a simple Drude model,

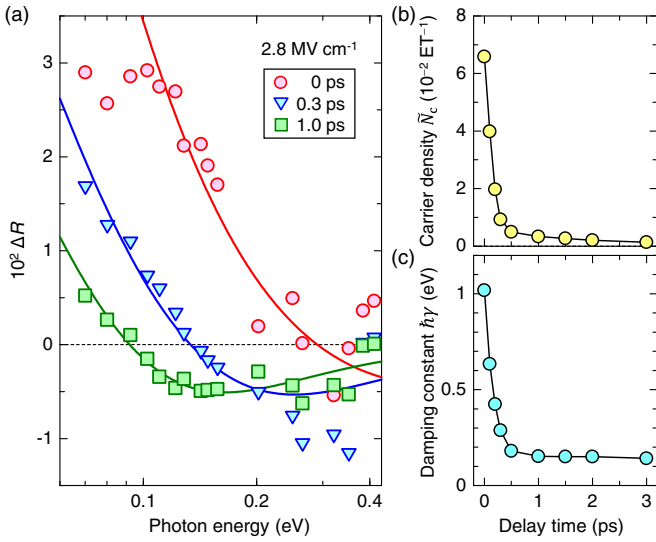


FIG. 6. Analyses of transient reflectivity changes with the Drude model. (a) $\Delta R(t_d)$ spectra in the mid-infrared region by the terahertz pulse with $E_{\text{THz}}(0) = 2.8 \text{ MV cm}^{-1}$. Color lines are the fitting curves calculated with the Drude model. Time characteristics of (b) the carrier density \tilde{N}_c and (c) the damping constant γ obtained from the fitting analyses.

with a decrease in photon energy from the higher-energy side, the reflectivity increases from the plasma frequency $\omega_p = \sqrt{\frac{e^2 N_c}{\epsilon_\infty \epsilon_0 m_{\text{eff}}}}$, where m_{eff} is the effective mass of carriers, N_c is the carrier density, ϵ_0 is the vacuum permittivity, and ϵ_∞ is the dielectric constant at higher photon energies. In the case of photoinduced metallization, the point where $\Delta R(t_d)$ crosses zero is just below $\hbar\omega_p$. Therefore, the observed monotonic decrease in $\hbar\omega_p$ over time can be explained by the decrease in the carrier number characteristic of the Drude response. Thus, the results suggest that the system exhibits a simple Drude response up to $t_d = 1 \text{ ps}$.

Figure 4(e) shows the time evolutions of the reflectivity changes $\Delta R(t_d)$ at 0.12 eV, reflecting the electric-field-induced carriers. For the terahertz pulse with $E_{\text{THz}}(0) = 0.25 \text{ MV cm}^{-1}$, no reflectivity change was observed (the blue line), whereas for the terahertz pulse with $E_{\text{THz}}(0) = 2.8 \text{ MV cm}^{-1}$, the $\Delta R(t_d)$ signal was positive near the time origin and turned negative at 0.4 ps. This negative signal gradually decayed over time. The sign inversion of the $\Delta R(t_d)$ signal occurs because the number of carriers decreases over time, and $\hbar\omega_p$ becomes smaller than the probe energy (0.12 eV). This behavior is also characteristic of a simple Drude response.

In Fig. 4(h), the magnitude of $\Delta R(0.2 \text{ ps})$ at 0.12 eV is plotted as a function of $E_{\text{THz}}(0)$. It can be seen that $\Delta R(0.2 \text{ ps})$ becomes slightly negative at $E_{\text{THz}}(0)$ from 0.9 to 1.6 MV cm^{-1} and then sharply increases at the larger $E_{\text{THz}}(0)$. This can be explained as follows. With an increase in $E_{\text{THz}}(0)$, $\hbar\omega_p$ increases owing to an increase in the carrier density. As $\hbar\omega_p$ approaches the probe energy from the lower energy side, the reflectivity change should be negative once. When $\hbar\omega_p$ exceeds the probe energy, the reflectivity change should become positive and increase with the further increase in $E_{\text{THz}}(0)$.

These features were reflected in the observed $E_{\text{THz}}(0)$ dependence of $\Delta R(0.2 \text{ ps})$, as shown in Fig. 4(h). The threshold behavior of the positive $\Delta R(0.2 \text{ ps})$ signals is like the electric field dependence of $\Delta R(1 \text{ ps})$ at 0.72 eV, shown in Fig. 4(g). These results again demonstrate that mobile carriers are generated by the quantum tunneling processes.

C. Analyses of transient mid-infrared reflectivity spectra with the Drude model

To obtain more detailed information regarding the dynamics of the electric-field-induced carriers, we analyzed the transient reflectivity spectra in the mid-infrared region using the simple Drude model. The fluence of a terahertz pulse gradually decays as it propagates in the single crystal of ET-F₂TCNQ; this is because part of the energy is used to generate carriers, in addition to the decay caused by weak phonon absorptions. Therefore, the generated carriers are expected to be distributed inhomogeneously along the depth direction of the crystal. To consider this situation, we simply assume that the carrier density $N_c(z)$ as a function of the depth z from the crystal surface is represented by the exponential formula $N_c(z) = N_c(0) \exp(-z/l_c)$. Here, l_c is the characteristic length that determines the distribution of the carriers, and $N_c(0)$ is the carrier density at the crystal surface. The carrier density averaged from the crystal surface to l_c along the depth direction \tilde{N}_c is represented as $\tilde{N}_c = (1-1/e)N_c(0)$. In this case, the complex dielectric constant $\tilde{\epsilon}(\omega, z)$ as a function of ω and z can be expressed as

$$\tilde{\epsilon}(\omega, z) = \epsilon_\infty - \frac{e^2}{\epsilon_0 m_{\text{eff}}} \frac{1}{\omega^2 + \gamma^2} \left(1 - i \frac{\gamma}{\omega} \right) N_c(z), \quad (2)$$

where γ , m_{eff} , and ϵ_∞ are the damping constant, effective mass of carriers, and dielectric constant at high frequencies, respectively. Using Eq. (2), the transient reflectivity spectra can be calculated analytically [54].

For simplicity, in our analyses, γ was assumed to be determined by the averaged carrier density \tilde{N}_c and was considered independent of the inhomogeneity of the carrier distribution along z . The effective mass m_{eff} of an electron carrier (doublon) and that of a hole carrier (holon) were not reported in ET-F₂TCNQ. In organic semiconductors [55,56] and 1D organic conductors with strongly correlated electron systems [57,58], it has been reported that m_{eff} is roughly equal to m_0 . Considering these studies, we assumed that the effective masses of electrons and holes in ET-F₂TCNQ are also equal to the free electron mass m_0 . Here, ϵ_∞ was determined to be 5.16 through an analysis of the steady-state reflectivity spectrum with the KK transformation. For the parameter l_c , we used 1 μm in all the time domains for up to 3 ps. Details of the evaluation procedure for the l_c value are presented in Sec. I of the Supplemental Material [59]. Adopting these parameter values, we performed fitting analyses of the transient reflectivity spectra $\Delta R(t_d)$, using Eq. (2). The fitting parameters were \tilde{N}_c and γ . Here, $N_c(z)$ in Eq. (2) can be uniquely determined from \tilde{N}_c using the relations $N_c(z) = N_c(0) \exp(-z/l_c)$ and $\tilde{N}_c = (1-1/e)N_c(0)$.

The solid lines in Fig. 6(a) denote the calculated $\Delta R(t_d)$ spectra, which almost entirely reproduce the experimental

$\Delta R(t_d)$ spectra, except for the data <0.1 eV at 0 ps. This discrepancy between the experimental and calculated $\Delta R(t_d)$ spectra can be related to the lack of temporal resolution in the measurements. In the mid-infrared region (<0.1 eV), many absorption lines originating from the water vapor and carbon dioxide in the atmosphere exist; these slightly increase the temporal width of the probe pulse, causing a decrease in the time resolution of the measurements <0.1 eV. As shown in Fig. 4(e), the reflectivity changes very quickly around the time origin, such that $\Delta R(t_d)$ at 0 ps can be suppressed <0.1 eV. For $t_d \geq 0.3$ ps, the reflectivity changes are relatively slow; hence, the lack of time resolution is expected to have no effect on the spectral shape of $\Delta R(t_d)$. This explains why the discrepancy between the experimental and calculated $\Delta R(t_d)$ spectra <0.1 eV only appears at $t_d = 0$ ps. Thus, we can consider that all three spectra can be almost entirely reproduced with the simple Drude model, which indicates that the carriers are not bound but instead move freely along the 1D molecular stacks.

Such a Drude response due to the electric-field-induced carriers can be interpreted by the spin-charge separation characteristic of 1D correlated electron systems with large U [62,63]. In half-filled Mott insulators, doped carriers move on the antiferromagnetic spin background. In 2D or three-dimensional systems, doped carriers cannot freely move due to the charge-spin coupling especially in the case of small number of carrier doping [64–66]. In contrast, in 1D systems, a carrier can move freely on the antiferromagnetic spin background because of the decoupling of charge and spin degrees of freedom irrespective of the magnitude of carrier density, and the spectral weight of the original Mott gap transition is necessarily transferred to the Drude component [63]. In fact, after the terahertz pulse excitation, the peak of the original ε_2 spectrum still exist, indicating that the Mott gap remains and doublons and holons generated in the upper and lower Hubbard bands, respectively. Because of the spin-charge separation, those carriers can freely move and contribute to the Drude response.

We performed the similar analyses of the ΔR spectra at various delay times t_d and evaluated the \tilde{N}_c and γ values, which are plotted in Figs. 6(b) and 6(c), respectively, as a function of t_d . \tilde{N}_c at the time origin ($t_d = 0$ ps) was 0.066 ET^{-1} . It decreased down to 0.01 ET^{-1} at $t_d = 0.3$ ps. Thereafter, the decay of \tilde{N}_c slowed considerably. The relatively slow decay characteristic of \tilde{N}_c for $t_d > 0.3$ ps is considerably like that observed in the transient change of the photocarrier density generated by 1.55-eV excitation previously reported [5]. These results suggest that the recombination rate of carriers decreases with the decrease of the carrier density and that Auger recombination might dominate the initial ultrafast decay process of carriers [60]. In fact, the important roles of Auger recombination in the ultrafast decay of photocarriers have been reported by the previous studies on the photoresponses of a 2D Mott insulator of Nd_2CuO_4 [14]. Thus, we really analysed the time characteristic of \tilde{N}_c in Fig. 6(b) assuming the Auger recombination process of photocarriers. The simulated time characteristic of \tilde{N}_c almost reproduced the experimental one, which are reported in Sec. II of the Supplemental Material [59]. These results indicate that the Auger recombination is important for the recombination mecha-

nism of carriers induced by the terahertz electric field in ET-F₂TCNQ.

As seen in Fig. 6(c), $\hbar\gamma$ is large, reaching 1 eV around the time origin; it rapidly decreases to approximately 0.15 eV within 0.3 ps, which corresponds to the rapid decrease of \tilde{N}_c . This indicates that the effect of carrier scattering becomes weaker with decreasing \tilde{N}_c and that the scattering between doublons and holons is responsible for the large $\hbar\gamma$ within 0.3 ps. This is consistent with the interpretation that Auger recombination dominates the rapid decay of \tilde{N}_c and the large $\hbar\gamma$ value immediately after the excitation can be ascribed to the active carrier scatterings, including the Auger recombination processes caused by the large number of carriers [14]. For $t_d > 0.3$ ps, γ is almost constant ($\hbar\gamma \sim 0.15$ eV), which is considered to correspond with the scattering rate of the isolated carriers, likely due to the intramolecular vibrations [45,67].

Finally, we discuss the excitonic effect on the electric field induced carrier generation. As mentioned in Secs. III A and III B, the previous studies have shown that the reflectivity peak around 0.7 eV in ET-F₂TCNQ is caused by excitons. However, as discussed in the previous part of this section, we considered that a strong terahertz pulse with $E_{\text{THz}}(0) = 2.8 \text{ MV cm}^{-1}$ generates unbound doublons and holons, and that their optical response follows the Drude model. To discuss the role of the excitonic effect in this carrier generation phenomenon, it is important to evaluate the electric field E_{ex} necessary to dissociate a doublon–holon pair constituting an exciton. Here, we assume that E_{ex} is expressed as $E_{\text{ex}} = \Delta_{\text{ex}}/(2e\xi_{\text{ex}})$, where Δ_{ex} is the binding energy of the exciton, and ξ_{ex} is the average distance between a doublon and holon in the exciton. This formula for E_{ex} is fundamentally the same as that used for the analysis of the electric field dependence of carrier generation [32]. The values of Δ_{ex} and ξ_{ex} can be derived from an analysis of the spectrum of the electric field induced reflectivity changes previously reported [45].

As briefly explained in Sec. III B, the analyses of the reflectivity change spectrum due to the third-order optical nonlinearity caused by a weak electric field in ET-F₂TCNQ were performed using the four-level model [45], which consists of the ground state $|0\rangle$, the lowest one-photon-allowed excitonic state with odd parity $|1\rangle$, the one-photon-forbidden excitonic state with even parity $|2\rangle$, and the second-lowest one-photon-allowed state with odd parity $|3\rangle$, corresponding to the continuum. The results showed that the binding energy Δ_{ex} of the lowest odd-parity exciton $|1\rangle$ was 156 meV [45]. The energy of the even-parity exciton $|2\rangle$ was 0.720 eV, whereas that of $|1\rangle$ was 0.694 eV. The splitting between states $|1\rangle$ and $|2\rangle$ was 26 meV. Namely, the energies of excitonic states $|1\rangle$ and $|2\rangle$ are almost degenerate, and their wavefunctions are very similar, except for their phases. As a result, the transition dipole moment between these two states, $\langle 1|x|2\rangle$, becomes significantly large and is evaluated to be 18 \AA [45]. This length corresponds to the spread of the doublon wave function along the 1D chain when a holon is located at the origin, because the spatial extensions of the wavefunctions of both $|1\rangle$ and $|2\rangle$ are almost identical. Therefore, it is a crude measure of the distance ξ_{ex} between a doublon and holon that constitutes the lowest exciton $|1\rangle$. The doublon–holon correlation length ξ ($=14.7 \text{ \AA}$) in the ground state, as obtained

by the fitting analysis of the electric field dependence of carrier generation, is shorter than ξ_{ex} (~ 18 Å). This is reasonable because ξ is scaled by the on-site Coulomb repulsion energy U determining the Mott gap energy. By contrast, ξ_{ex} is scaled by the intersite Coulomb repulsion energy V ($< U$), although an advanced theoretical study is necessary to demonstrate its quantitative validity. Using the relation $E_{\text{ex}} = \Delta_{\text{ex}}/(2e\xi_{\text{ex}})$, E_{ex} was determined to be ~ 0.43 MV cm $^{-1}$. This electric field magnitude is considerably lower than the threshold electric field for carrier generation owing to quantum tunneling processes, i.e., $E_{\text{th}} = 2.37$ MV cm $^{-1}$. Therefore, a doublon-holon pair generated by a quantum tunneling process under an electric field comparable with or larger than E_{th} should instantaneously dissociate into an unbound doublon and holon. Thus, the excitonic effect does not affect the carrier generation process under a terahertz pulse observed in this paper.

D. Spectra of transient dielectric constants derived by KK transformation

As mentioned in Sec. III C, the spectra of the transient reflectivity changes $\Delta R(t_d)$ in the mid-infrared region caused by the application of an electric field with a terahertz pulse were well reproduced by the Drude model. Therefore, we can extrapolate the $\Delta R(t_d)$ spectra to the low-energy region below the lower energy bound of the measured region and calculate the transient complex dielectric constant $\tilde{\epsilon}(\omega, t_d)$ for all the photon energy regions from 0 to 1.1 eV as follows.

In a medium with a uniform electronic state, like the steady state of this compound, the $\tilde{\epsilon}(\omega)$ spectra can be obtained from the reflectivity spectrum using the KK transformation. However, as mentioned in Sec. III C, the excited states generated by a terahertz pulse are not spatially uniform. Therefore, $\tilde{\epsilon}(\omega)$ cannot be obtained directly using the same method as that for the steady state. To overcome this, we referred to a previous work [68], where the $\tilde{\epsilon}(\omega)$ spectra were numerically calculated using the following method. In that study, the number of photocarriers was assumed to decrease exponentially along the depth direction (z) of the crystal. Therefore, using the parameter l_c , the complex dielectric constant at depth z from the crystal surface $\tilde{\epsilon}(z, \omega)$ can be expressed as follows:

$$\tilde{\epsilon}(z, \omega) = \tilde{\epsilon}_{\text{tr}}(\omega) \exp\left(-\frac{z}{l_c}\right) + \tilde{\epsilon}_{\text{st}}(\omega) \left[1 - \exp\left(-\frac{z}{l_c}\right)\right]. \quad (3)$$

Here, $\tilde{\epsilon}_{\text{st}}(\omega)$ and $\tilde{\epsilon}_{\text{tr}}(\omega)$ are the complex dielectric constants of the steady state and photoexcited state at the crystal surface, respectively. Given these complex dielectric constants, the complex amplitude reflectivity $\tilde{r}^{\text{cal}}(\omega)$ can be calculated numerically. By assuming an appropriate set of the real and imaginary parts of $\tilde{\epsilon}_{\text{tr}}(\omega)$ as the initial values, we calculated $\tilde{r}^{\text{cal}}(\omega)$. Subsequently, we compared $\tilde{r}^{\text{cal}}(\omega)$ with the complex amplitude reflectivity $\tilde{r}^{\text{ex}}(\omega)$, which was obtained from the experimental $\Delta R(t_d)$ spectrum via the KK transformation. Moreover, $\tilde{\epsilon}_{\text{tr}}(\omega)$ was updated such that $\Delta\tilde{r}(\omega) = \tilde{r}^{\text{ex}}(\omega) - \tilde{r}^{\text{cal}}(\omega)$ decreases. By repeating these procedures, we obtain $\tilde{\epsilon}_{\text{tr}}(\omega)$. For the KK transformation of the transient reflectivity spectra mentioned above, $R(\omega) + \Delta R(\omega)$ below the lower energy bound of the measurable region (0.1 eV at $t_d = 0$ ps and 0.065 eV at $t_d = 0.3$ and 1 ps) was extrapolated using

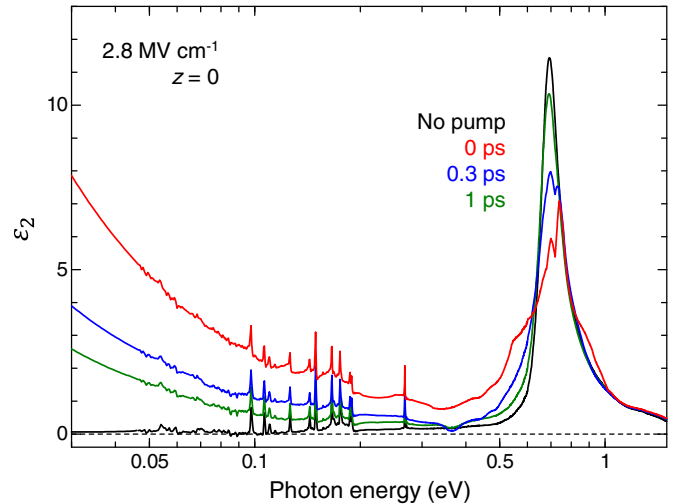


FIG. 7. The spectra of the imaginary part of the transient complex dielectric constant $\tilde{\epsilon}_{\text{tr}}(\omega)$. Color lines show ϵ_2 spectra at the crystal surface ($z = 0$) obtained from the $[R + \Delta R(t_d)]$ spectra with $E_{\text{THz}}(0) = 2.8$ MV cm $^{-1}$ with the method mentioned in Sec. III D. The black solid line shows the original ϵ_2 spectrum [the same as the black line shown in Fig. 3(b)].

the reflectivity values obtained by the fitting analyses of the $\Delta R(t_d)$ spectra, as mentioned in Sec III C, whereas that above the higher energy bound of the measured region (1.15 eV) was set to be equal to the original reflectivity $R(\omega)$.

Figure 7 shows the spectra of the imaginary part of $\tilde{\epsilon}_{\text{tr}}(\omega)$ obtained in this manner with respect to the logarithmic scale of the photon energy. The solid black line indicates the original ϵ_2 spectrum. Immediately after the excitation with the terahertz pulse, the oscillator strength of the exciton absorption peak ~ 0.7 eV decreases; this is termed as a bleaching signal. The decreased spectral weight was transferred to the low-energy region, which is a general phenomenon that occurs when carriers are injected into a Mott insulator. The slight increases in ϵ_2 on both sides of the bleaching signal caused by carrier generation are ascribed to the third-order nonlinear optical effect, as mentioned in Sec. III B. Note that almost the entire decreased spectral weight around the original absorption peak is transferred to the Drude component, and no midgap absorptions appear. This also originates from the spin-charge separation characteristics of 1D correlated electron systems with a large U [62,63]. In addition, even after the terahertz pulse excitation, the peak of the original ϵ_2 spectrum still exists, which suggests that the Mott gap remains and the doublons and holons generated in the upper and lower Hubbard bands, respectively, are contributed to the Drude response.

E. Evaluations of energy efficiency of electric-field-induced carrier generations

It is important to compare the energy required to generate carriers by a photoexcitation with that by a terahertz pulse excitation in terms of an exploration of the efficient carrier generation process and an efficient insulator-metal transition. In the case of the optical excitation, the value of the absorption

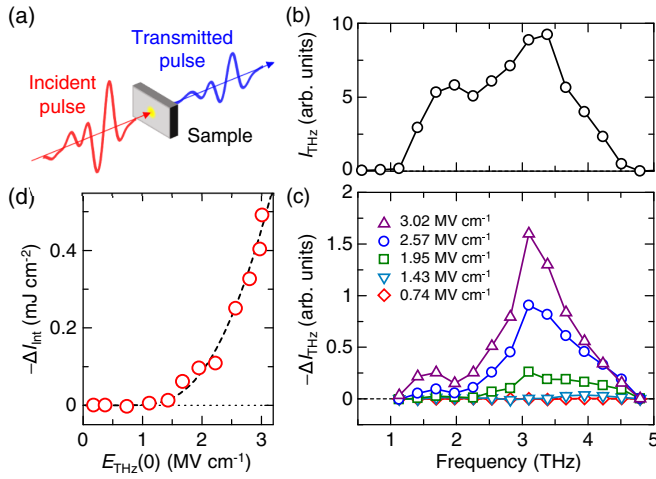


FIG. 8. Nonlinear absorptions of terahertz pump pulses. (a) A schematic configuration of terahertz absorption measurements. (b) Fourier power spectrum of the terahertz pulse $I_{\text{THz}}(\omega)$, which is the same as that shown in Fig. 2(b). (c) Nonlinear increases of absorbed intensities of terahertz pulses $-\Delta I_{\text{THz}}(\omega)$, with several typical $E_{\text{THz}}(0)$ values. (d) $E_{\text{THz}}(0)$ dependence of the integrated nonlinear absorption intensities $-\Delta I_{\text{int}}$. The broken line shows the fitting curve with the same value of the threshold electric field E_{th} as shown by the green solid line in Fig. 4(g).

coefficient provides a precise evaluation of the depth region from the crystal surface at which photons are absorbed and carriers are generated. In the case of the terahertz pulse excitation, in which carriers are dissociated by its electric field component, there must be also a loss of energy because the terahertz pulse does some work. However, it is difficult to theoretically determine the energy of the terahertz pulse used for the carrier generations because the quantum tunneling process due to the electric field occurs in a highly nonlinear manner with respect to the electric field strength. Therefore, in this paper, we tried to obtain it experimentally.

When $E_{\text{THz}}(0)$ is small, the transmission spectrum does not depend on $E_{\text{THz}}(0)$ and the terahertz pulse decays within the crystal, according to the linear absorption coefficient due to the phonon absorptions [see Fig. 3(b)]. When $E_{\text{THz}}(0)$ is increased above E_{th} , a nonlinear increase in the absorption of the terahertz pulse should occur because the energy of the terahertz pulse is used for carrier generations via the quantum tunneling processes. Therefore, by measuring the terahertz electric field dependence of the transmittance of the terahertz pulse, as illustrated in Fig. 8(a), the energy of the terahertz pulse used for carrier generations can be evaluated.

Figures 8(b) and 8(c) show the power spectrum of the incident terahertz pulse $I_{\text{THz}}(\omega)$ and the nonlinear increase in the absorption intensity of the terahertz pulse $-\Delta I_{\text{THz}}(\omega)$ for several typical $E_{\text{THz}}(0)$ values of the terahertz pulse, respectively. For $E_{\text{THz}}(0) < 1.5 \text{ MV cm}^{-1}$, $-\Delta I_{\text{THz}}(\omega)$ is negligibly small, indicating that no nonlinear absorption occurs. However, when the electric field is 1.9 MV cm^{-1} or higher, $-\Delta I_{\text{THz}}(\omega)$ increases nonlinearly. The open circles in Fig. 8(d) denote the integrated intensities of the nonlinear absorptions of terahertz pulses $-\Delta I_{\text{int}}$ as a function of $E_{\text{THz}}(0)$, which increases

$> 1.5 \text{ MV cm}^{-1}$. This behavior is very similar to the reflectivity change at 1 ps, $\Delta R(1 \text{ ps})$, in the near-infrared region, as shown by the green triangles in Fig. 4(g), which reflects the carrier generation caused by the quantum tunneling processes. Furthermore, as shown by the broken line in Fig. 8(d), the $E_{\text{THz}}(0)$ dependence of $-\Delta I_{\text{int}}$ (the open circles) is well reproduced by the same equation $E_{\text{THz}}(0) \exp[-\pi E_{\text{th}}/E_{\text{THz}}(0)]$ with the same parameter value of $E_{\text{th}} = 2.37 \text{ MV cm}^{-1}$ as that used for Fig. 4(g).

Optical pump–reflectivity probe spectroscopy of ET-F₂TCNQ was previously performed by the resonant excitation of excitons with a 0.7-eV pulse [45] and by the higher energy excitation with a 1.55-eV pulse [5]. Those studies showed that photocarriers are less likely to be generated due to the excitonic effect when ET-F₂TCNQ was excited with a 0.7-eV pulse, whereas they are more efficient and a Drude response in the mid-infrared region was observed when excited with a 1.55-eV pulse [5]. Therefore, we used the results for the 1.55-eV excitation to compare the energy efficiency for carrier generations with that for the terahertz pulse excitation. In the case of the terahertz pulse excitation with $E_{\text{THz}}(0) = 2.8 \text{ MV cm}^{-1}$, the excitation fluence is 1.33 mJ cm^{-2} . Considering the amount of nonlinear absorption [Fig. 8(d)], the energy used to generate carriers within $l_c = 1 \text{ }\mu\text{m}$ is 0.36 mJ cm^{-2} , whereas the amount of the sum of doublons and holons generated within l_c , $\tilde{N}_c l_c$, is $1.10 \times 10^{16} \text{ cm}^{-2}$. In the case of the 1.55-eV photoexcitation, the experiments were performed under two types of photoexcitation conditions: weak photoexcitation with 0.116 mJ cm^{-2} and strong photoexcitation with 3.67 mJ cm^{-2} [5]. The Drude responses were observed under both these excitation conditions. In the weak and strong photoexcitation conditions, the energies absorbed within the absorption depth ($0.58 \text{ }\mu\text{m}$) are 0.073 and 2.32 mJ cm^{-2} , and the amount of generated carriers within the same region are 4.97×10^{14} and $5.74 \times 10^{15} \text{ cm}^{-2}$, respectively. Based on these parameter values, the energy required to generate a doublon-holon pair using a terahertz pulse was estimated to be $\frac{1}{5}$ and $\frac{1}{13}$ of that during weak and strong photoexcitation, respectively.

We conjecture that the difference in energy efficiency between the weak and strong photoexcitation conditions originates from two factors. The first is the absorption saturation in the latter. The absorption coefficient for 1.55-eV light is considerably larger than that for the terahertz pulse; hence, absorption saturation is likely to occur, and the effective excitation fluence decreases under strong photoexcitation. The second factor is that Auger recombination occurs more actively under strong photoexcitation than under weak photoexcitation, and many photocarriers recombine within the temporal width of the pump pulse, that is, 130 fs. It has been reported that photocarriers recombine within a time resolution of 180 fs [5]. Based on these estimations, it is natural to consider that the energy efficiency of carrier generation by a terahertz pulse is at least five times greater than that by photoexcitation at 1.55 eV.

Finally, we briefly discuss the difference in the energy efficiencies of carrier generation via terahertz pulse excitation and photoexcitation. In previously reported photoexcitation measurements [5], the pump photon energy was 1.55 eV, which is considerably larger than the Mott gap energy of

~ 0.7 eV. Therefore, the excess energy (~ 0.85 eV) will not be used for photocarrier generation and is likely transferred to the phonons. However, this alone does not explain the fivefold (or higher) energy efficiency difference between terahertz pulse excitation and photoexcitation. Another possible reason is the activation of doublon-holon recombination during the relaxation process of the high-energy photoexcited state initially created by photoexcitation. If photocarrier recombination occurs within the temporal width of the excitation pulse, that is, within the time resolution, the effective efficiency of carrier generation evaluated based on transient spectral changes would decrease. Under the electric field of a terahertz pulse, doublons and holons tend to be spatially separated and do not have large excess energies; hence, the carrier recombination rate might be suppressed, as compared with that in the photoexcitation case. Note that Auger recombination seems to remain effective in the terahertz pulse excitation case, as mentioned in Sec. III C. Judging from the facts that, in the weak photoexcitation with 1.55 eV, Auger recombination of carriers hardly occurs and the energy required to generate a doublon-holon pair using a terahertz pulse was estimated to be $\frac{1}{5}$ of that during the weak photoexcitation, we can conclude that the energy efficiency for carrier generations by a terahertz pulse excitation is actually at least five times higher than that by a photoexcitation with 1.55 eV.

F. Comparison of electric-field-induced carrier generations in ET-F₂TCNQ with related phenomena

In this section, we compare the electric-field-induced metallization of the 1D Mott insulator ET-F₂TCNQ by a terahertz pulse observed in this paper with other related electric-field-induced phenomena previously reported. Carrier generation and metallization using a terahertz pulse excitation in Mott insulators have been studied in a 2D Mott insulator of an organic molecular compound κ -(ET)₂Cu[N(CN)₂]Br [38]. In this compound, the 2D arrangement of ET dimers with one hole per ET dimer forms a half-filled electronic system. A thin single crystal of this compound cooled on a diamond substrate becomes a 2D Mott insulator with a Mott gap energy of ~ 30 meV at low temperatures. When this compound is irradiated with a terahertz pulse, the absorption spectrum in the mid-infrared region changes drastically at an electric field amplitude > 64 kV cm⁻¹, which is the threshold electric field. The absorption change is in good agreement with the differential absorption spectrum between the high-temperature metallic phase and low-temperature Mott insulator phase, which demonstrates that the system is metallized by a terahertz electric field. In the electric-field-induced metallization of this compound, the absorption change appears over a wide energy range from 0.8 to 0.1 eV, the lower bound of the measurement range and cannot be explained as a simple Drude response. It is reasonable since, in a 2D Mott insulator such as κ -(ET)₂Cu[N(CN)₂]Br, the charge and spin degrees of freedom are coupled and a metallic state shows a spectrum different from the simple Drude response [69]. Since ET-F₂TCNQ investigated in this paper is a 1D Mott insulator, the charge and spin degrees of freedom are decoupled, as mentioned earlier, and carriers show a simple Drude response [63]. The correlation length ξ , which represents the

average distance between doublon and holon, is ~ 23 Å in κ -(ET)₂Cu[N(CN)₂]Br, which is about three times the distance between the adjacent dimers. On the other hand, for ET-F₂TCNQ, ξ is ~ 15 Å, which is ~ 2.5 times the molecular spacing along the molecular stacking axis a . Thus, the reason why ξ in ET-F₂TCNQ with the Mott gap energy of 0.7 eV is comparable with that in κ -(ET)₂Cu[N(CN)₂]Br with the Mott gap energy of only 30 meV is that the value of the transfer integral between the adjacent molecules in ET-F₂TCNQ is ~ 0.2 eV [70], whereas the transfer integrals between the adjacent dimers are much smaller, being ~ 30 or 70 meV for κ -(ET)₂Cu[N(CN)₂]Br [38].

In ET-F₂TCNQ, an electronic state control by a mid-infrared pulse excitation has also been reported [35,36]. In that study, the polarization of the mid-infrared pulse is not along the molecular stacking axis a but along the b axis, which is perpendicular to the a axis. This polarization excites infrared-active intramolecular vibrations in each ET molecule, which modulates the on-site Coulomb repulsion energy U of the ET molecule at twice the vibrational frequency. As a result, a modulation of the energy of the Mott gap transition (exciton absorption) at 0.7 eV was observed. In the excitation by this b -axis polarized mid-infrared pulse, no carrier generation by quantum tunneling processes occurs. This can be explained in the following way. As shown in Figs. 1(a) and 1(b), carrier generation by an electric field occurs when the band is tilted in the direction of the electric field. However, in the b -axis direction, a molecule which is in close proximity to the ET molecule, is an isolated F₂TCNQ molecule, and the transfer integral between ET and F₂TCNQ is 5.5 meV, which is extremely small compared with the transfer integral (~ 0.2 eV) between ET molecules in the ET stacks along the a axis [70], and the overlap of wave functions between ET molecules in different ET stacks can be neglected. Therefore, it is reasonable to consider that no band transport of carriers occurs in the b -axis direction. Indeed, no electronic transitions are observed for the electric field of lights polarized parallel to the b axis [37,45]. Thus, carrier generations via the quantum tunneling processes shown in Figs. 1(a) and 1(b) are not expected to occur. In fact, no sign of carrier generations has been observed in the experiments with a mid-infrared pulse excitation in the b -axis direction [35,36].

Next, we will compare the results of ET-F₂TCNQ in this paper with those of VO₂ in the previous study using the mid-infrared pulse excitation [34]. VO₂ shows an insulator-metal transition with a large structural change at 340 K below which the insulator state is stabilized by the strong dimerization of V ions. Although this compound is not a pure Mott insulator, it has been reported that a mid-infrared pulse generates carriers via the quantum tunneling processes, which destabilize the V-V dimers and cause a structural change to convert the compound to a metallic state. From the magnitude of the threshold electric field where the metallization occurs, the correlation length ξ between electron and hole was estimated to be 2.6 Å. This distance is shorter than the distance between the adjacent V-V dimers (2.65 Å) [71,72]. The energy gap in the insulator phase of VO₂ is ~ 0.6 eV, which is comparable with the energy gap of ET-F₂TCNQ, ~ 0.7 eV. Here, ξ in VO₂ is $\frac{1}{7}$ of ξ in ET-F₂TCNQ. When we divided ξ by the distance between the adjacent units (5.8 Å in ET-F₂TCNQ [37] and 2.65 Å in

VO₂), the effective ratio is equal to $\sim \frac{1}{3}$. Such a small ξ in VO₂ is probably because, in the structure of the insulator phase, the *d* electrons of the V ions are strongly localized in the V-V dimers due to the small overlap of the wave functions between the adjacent V-V dimers. In addition, VO₂ in the low-temperature insulator phase is not a pure Mott insulator, and a structural change will be required for the metallization [8,73]. For the structural change, a large carrier density will also be required. It is therefore possible that the apparent threshold electric field for the carrier generation was enhanced, and ξ was estimated to be smaller than the real value in VO₂.

IV. SUMMARY

To summarize, the electronic state change in a 1D Mott insulator due to a strong electric field was investigated by irradiating an organic molecular compound ET-F₂TCNQ with a terahertz pulse featuring an electric field amplitude of up to ~ 3 MV cm⁻¹. Analyses of the transient changes in the reflectivity spectrum and its electric field dependence revealed that carrier generation occurs via the quantum tunneling pro-

cess. We carefully compared the energy efficiencies of carrier generation via terahertz pulse excitation and photoexcitation of 1.55 eV beyond the optical gap. The analysis results indicated that the energy efficiency of carrier generation in the former was at least five times larger than that in the latter. Thus, terahertz pulse excitation is an effective method for creating carriers in a solid, especially in materials where carrier doping via elemental substitution is difficult. Therefore, the proposed method of carrier doping using a terahertz pulse can be applied to various complex materials.

ACKNOWLEDGMENTS

We thank T. Otaki and N. Kida for enlightening discussions. This paper was supported in part by the Japan Society for the Promotion of Science (Projects No. JP18H01166, No. JP20K03801, and No. JP21H04988) and by CREST (Grant No. JPMJCR1661), Japan Science and Technology Agency (JST). N.T. was supported by JST SPRING (Grant No. JPMJSP2108).

-
- [1] M. Imada, A. Fujimori, and Y. Tokura, Metal insulator transitions, *Rev. Mod. Phys.* **70**, 1039 (1998).
- [2] J. G. Bednorz and K. A. Müller, Possible high T_c superconductivity in the Ba–La–Cu–O system, *Z. Phys. B* **64**, 189 (1986).
- [3] Y. Tokura, H. Takagi, and S. Uchida, A superconducting copper oxide compound with electrons as the charge carriers, *Nature (London)* **337**, 345 (1989).
- [4] S. Iwai, M. Ono, A. Maeda, H. Matsuzaki, H. Kishida, H. Okamoto, and Y. Tokura, Ultrafast Optical Switching to a Metallic State by Photoinduced Mott Transition in a Halogen-Bridged Nickel-Chain Compound, *Phys. Rev. Lett.* **91**, 057401 (2003).
- [5] H. Okamoto, H. Matsuzaki, T. Wakabayashi, Y. Takahashi, and T. Hasegawa, Photoinduced Metallic State Mediated by Spin-Charge Separation in a One-Dimensional Organic Mott Insulator, *Phys. Rev. Lett.* **98**, 037401 (2007).
- [6] H. Okamoto, T. Miyagoe, K. Kobayashi, H. Uemura, H. Nishioka, H. Matsuzaki, A. Sawa, and Y. Tokura, Ultrafast charge dynamics in photoexcited Nd₂CuO₄ and La₂CuO₄ cuprate compounds investigated by femtosecond absorption spectroscopy, *Phys. Rev. B* **82**, 060513(R) (2010).
- [7] H. Okamoto, T. Miyagoe, K. Kobayashi, H. Uemura, H. Nishioka, H. Matsuzaki, A. Sawa, and Y. Tokura, Photoinduced transition from Mott insulator to metal in the undoped cuprates Nd₂CuO₄ and La₂CuO₄, *Phys. Rev. B* **83**, 125102 (2011).
- [8] A. Cavalleri, C. Tóth, C. W. Siders, J. A. Squier, F. Ráksi, P. Forget, and J. C. Kieffer, Femtosecond Structural Dynamics in VO₂ during an Ultrafast Solid-Solid Phase Transition, *Phys. Rev. Lett.* **87**, 237401 (2001).
- [9] M. Chollet, L. Guerin, N. Uchida, S. Fukaya, H. Shimoda, T. Ishikawa, K. Matsuda, T. Hasegawa, A. Ota, H. Yamochi *et al.*, Gigantic photoresponse in 1/4-filled-band organic salt (EDO-TTF)₂PF₆, *Science* **307**, 86 (2005).
- [10] M. Matsubara, Y. Okimoto, T. Ogasawara, Y. Tomioka, H. Okamoto, and Y. Tokura, Ultrafast Photoinduced Insulator-Ferromagnet Transition in the Perovskite Manganite Gd_{0.55}Sr_{0.45}MnO₃, *Phys. Rev. Lett.* **99**, 207401 (2007).
- [11] D. Polli, M. Rini, S. Wall, R. W. Schoenlein, Y. Tomioka, Y. Tokura, G. Cerullo, and A. Cavalleri, Coherent orbital waves in the photo-induced insulator–metal dynamics of a magnetoresistive manganite, *Nature Mater.* **6**, 643 (2008).
- [12] R. Yusupov, T. Mertelj, V. V. Kabanov, S. Brazovskii, P. Kusar, J.-H. Chu, I. R. Fisher, and D. Mihailovic, Coherent dynamics of macroscopic electronic order through a symmetry breaking transition, *Nature Phys.* **6**, 681 (2010).
- [13] M. Cammarata, R. Bertoni, M. Lorenc, H. Cailleau, S. Di Matteo, C. Mauriac, S. F. Matar, H. Lemke, M. Chollet, S. Ravy *et al.*, Sequential Activation of Molecular Breathing and Bending During Spin-Crossover Photoswitching Revealed by Femtosecond Optical and X-Ray Absorption Spectroscopy, *Phys. Rev. Lett.* **113**, 227402 (2014).
- [14] T. Miyamoto, Y. Matsui, T. Terashige, T. Morimoto, N. Sono, H. Yada, S. Ishihara, Y. Watanabe, S. Adachi, T. Ito *et al.*, Probing ultrafast spin-relaxation and precession dynamics in a cuprate Mott insulator with seven-femtosecond optical pulses, *Nat. Commun.* **9**, 3948 (2018).
- [15] J. Hebling, G. Almási, I. Z. Kozma, and J. Kuhl, Velocity matching by pulse front tilting for large-area THz-pulse generation, *Opt. Express* **10**, 1161 (2002).
- [16] H. Hirori, A. Doi, F. Blanchard, and K. Tanaka, Single-cycle terahertz pulses with amplitudes exceeding 1 MV/cm generated by optical rectification in LiNbO₃, *Appl. Phys. Lett.* **98**, 091106 (2011).
- [17] T. Kampfrath, K. Tanaka, and K. A. Nelson, Resonant and nonresonant control over matter and light by intense terahertz transients, *Nature Photon.* **7**, 680 (2013).
- [18] T. Kampfrath, A. Sell, G. Klatt, A. Pashkin, S. Mährlein, T. Dekorsy, M. Wolf, M. Fiebig, A. Leitenstorfer, and R. Huber, Coherent terahertz control of antiferromagnetic spin waves, *Nature Photon.* **5**, 31 (2011).
- [19] T. Kubacka, J. A. Johnson, M. C. Hoffmann, C. Vicario, S. de Jong, P. Beaud, S. Grübel, S.-W. Huang, L. Huber, L. Patthey *et al.*, Large-amplitude spin dynamics driven by a THz pulse in resonance with an electromagnon, *Science* **343**, 1333 (2014).

- [20] E. A. Mashkovich, K. A. Grishunin, R. M. Dubrovin, A. K. Zvezdin, R. V. Pisarev, and A. V. Kimel, Terahertz light-driven coupling of antiferromagnetic spins to lattice, *Science* **374**, 1608 (2021).
- [21] T. Miyamoto, H. Yada, H. Yamakawa, and H. Okamoto, Ultrafast modulation of polarization amplitude by terahertz fields in electronic-type organic ferroelectrics, *Nat. Commun.* **4**, 2586 (2013).
- [22] F. Chen, J. Goodfellow, S. Liu, I. Grinberg, M. C. Hoffmann, A. R. Damodaran, Y. Zhu, P. Zalden, X. Zhang, I. Takeuchi *et al.*, Ultrafast terahertz gating of the polarization and giant nonlinear optical response in BiFeO₃ thin films, *Adv. Mater.* **27**, 6371 (2015).
- [23] T. Morimoto, T. Miyamoto, H. Yamakawa, T. Terashige, T. Ono, N. Kida, and H. Okamoto, Terahertz-Field-Induced Large Macroscopic Polarization and Domain-Wall Dynamics in an Organic Molecular Dielectric, *Phys. Rev. Lett.* **118**, 107602 (2017).
- [24] X. Li, T. Qiu, J. Zhang, E. Baldini, J. Lu, A. M. Rappe, and K. A. Nelson, Terahertz field-induced ferroelectricity in quantum paraelectric SrTiO₃, *Science* **364**, 1079 (2019).
- [25] M. C. Hoffmann, J. Hebling, H. Y. Hwang, K.-L. Yeh, and K. A. Nelson, Impact ionization in InSb probed by terahertz pump-terahertz probe spectroscopy, *Phys. Rev. B* **79**, 161201(R) (2009).
- [26] H. Hirori, M. Nagai, and K. Tanaka, Excitonic interactions with intense terahertz pulses in ZnSe/ZnMgSSe multiple quantum wells, *Phys. Rev. B* **81**, 081305(R) (2010).
- [27] M. Liu, H. Y. Hwang, H. Tao, A. C. Strikwerda, K. Fan, G. R. Keiser, A. J. Sternbach, K. G. West, S. Kittiwatanakul, J. Lu *et al.*, Terahertz-field-induced insulator-to-metal transition in vanadium dioxide metamaterial, *Nature (London)* **487**, 345 (2012).
- [28] R. Matsunaga, N. Tsuji, H. Fujita, A. Sugioka, K. Makise, Y. Uzawa, H. Terai, Z. Wang, H. Aoki, and R. Shimono, Light-induced collective pseudospin precession resonating with Higgs mode in a superconductor, *Science* **345**, 1145 (2014).
- [29] F. Giorgianni, T. Cea, C. Vicario, C. P. Hauri, W. K. Withanage, X. Xi, and L. Benfatto, Leggett mode controlled by light pulses, *Nat. Phys.* **15**, 341 (2019).
- [30] T. Oka and H. Aoki, Ground-State Decay Rate for the Zener Breakdown in Band and Mott Insulators, *Phys. Rev. Lett.* **95**, 137601 (2005).
- [31] M. Eckstein, T. Oka, and P. Werner, Dielectric Breakdown of Mott Insulators in Dynamical Mean-Field Theory, *Phys. Rev. Lett.* **105**, 146404 (2010).
- [32] T. Oka, Nonlinear doublon production in a Mott insulator: Landau-Dykhne method applied to an integrable model, *Phys. Rev. B* **86**, 075148 (2012).
- [33] C. Zener, A theory of the electrical breakdown of solid dielectrics, *Proc. R. Soc. Lond. A* **145**, 523 (1934).
- [34] B. Mayer, C. Schmidt, A. Grupp, J. Bühler, J. Oelmann, R. E. Marvel, R. F. Haglund, Jr., T. Oka, D. Brida, A. Leitenstorfer *et al.*, Tunneling breakdown of a strongly correlated insulating state in VO₂ induced by intense multiterahertz excitation, *Phys. Rev. B* **91**, 235113 (2015).
- [35] S. Kaiser, S. R. Clark, D. Nicoletti, G. Cotugno, R. I. Tobey, N. Dean, S. Lupi, H. Okamoto, T. Hasegawa, D. Jaksch *et al.*, Optical Properties of a Vibrationally Modulated Solid State Mott Insulator, *Sci. Rep.* **4**, 3823 (2014).
- [36] R. Singla, G. Cotugno, S. Kaiser, M. Först, M. Mitrano, H. Y. Liu, A. Cartella, C. Manzoni, H. Okamoto, T. Hasegawa *et al.*, THz-Frequency Modulation of the Hubbard U in an Organic Mott Insulator, *Phys. Rev. Lett.* **115**, 187401 (2015).
- [37] T. Hasegawa, S. Kagoshima, T. Mochida, S. Sugiura, and Y. Iwasa, Electronic states and anti-ferromagnetic order in mixed-stack charge-transfer compound (BEDT-TTF)(F₂TCNQ), *Solid State Commun.* **103**, 489 (1997).
- [38] H. Yamakawa, T. Miyamoto, T. Morimoto, T. Terashige, H. Yada, N. Kida, M. Suda, H. M. Yamamoto, R. Kato, K. Miyagawa *et al.*, Mott transition by an impulsive dielectric breakdown, *Nature Mater.* **16**, 1100 (2017).
- [39] L. Mütter, F. D. J. Brunner, Z. Yang, M. Jazbinšek, and P. Günter, Linear and nonlinear optical properties of the organic crystal DSTMS, *J. Opt. Soc. Am. B* **24**, 2556 (2007).
- [40] C. Ruchert, C. Vicario, and C. P. Hauri, Spatiotemporal Focusing Dynamics of Intense Supercontinuum THz Pulses, *Phys. Rev. Lett.* **110**, 123902 (2013).
- [41] M. Shalaby and C. P. Hauri, Demonstration of a low-frequency three-dimensional terahertz bullet with extreme brightness, *Nat. Commun.* **6**, 5976 (2015).
- [42] D. S. Sitnikov, S. A. Romashevskiy, A. V. Ovchinnikov, O. V. Chefonov, A. B. Savel'ev, and M. B. Agranat, Estimation of THz field strength by an electro-optic sampling technique using arbitrary long gating pulses, *Laser Phys. Lett.* **16**, 115302 (2019).
- [43] D. J. Cook and R. M. Hochstrasser, Intense terahertz pulses by four-wave rectification in air, *Opt. Lett.* **25**, 1210 (2000).
- [44] K. Y. Kim, J. H. Glowina, A. J. Taylor, and G. Rodriguez, Terahertz emission from ultrafast ionizing air in symmetry-broken laser fields, *Opt. Express* **15**, 4577 (2007).
- [45] T. Miyamoto, T. Kakizaki, T. Terashige, D. Hata, H. Yamakawa, T. Morimoto, N. Takamura, H. Yada, Y. Takahashi, T. Hasegawa *et al.*, Biexciton in one-dimensional Mott insulators, *Commun. Phys.* **2**, 131 (2019).
- [46] T. Yamaguchi, K. Iwano, T. Miyamoto, N. Takamura, N. Kida, Y. Takahashi, T. Hasegawa, and H. Okamoto, Excitonic optical spectra and energy structures in a one-dimensional Mott insulator demonstrated by applying a many-body Wannier functions method to a charge model, *Phys. Rev. B* **103**, 045124 (2021).
- [47] P. N. Butcher and D. Cotter, *The Elements of Nonlinear Optics* (Cambridge University Press, Cambridge, 1990).
- [48] H. Yada, T. Miyamoto, and H. Okamoto, Terahertz-field-driven sub-picosecond optical switching enabled by large third-order optical nonlinearity in a one-dimensional Mott insulator, *Appl. Phys. Lett.* **102**, 091104 (2013).
- [49] T. Terashige, T. Ono, T. Miyamoto, T. Morimoto, H. Yamakawa, N. Kida, T. Ito, T. Sasagawa, T. Tohyama, and H. Okamoto, Doublon-holon pairing mechanism via exchange interaction in two-dimensional cuprate Mott insulators, *Sci. Adv.* **5**, eaav2187 (2019).
- [50] H. Hirori, K. Shinokita, M. Shirai, S. Tani, Y. Kadoya, and K. Tanaka, Extraordinary carrier multiplication gated by a picosecond electric field pulse, *Nat. Commun.* **2**, 594 (2011).
- [51] H. Kishida, H. Matsuzaki, H. Okamoto, T. Manabe, M. Yamashita, Y. Taguchi, and Y. Tokura, Gigantic optical nonlinearity in one-dimensional Mott-Hubbard insulators, *Nature (London)* **405**, 929 (2000).

- [52] Y. Mizuno, K. Tsutsui, T. Tohyama, and S. Maekawa, Nonlinear optical response and spin-charge separation in one-dimensional Mott insulators, *Phys. Rev. B* **62**, R4769(R) (2000).
- [53] M. Ono, K. Miura, A. Maeda, H. Matsuzaki, H. Kishida, Y. Taguchi, Y. Tokura, M. Yamashita, and H. Okamoto, Linear and nonlinear optical properties of one-dimensional Mott insulators consisting of Ni-halogen chain and CuO-chain compounds, *Phys. Rev. B* **70**, 085101 (2004).
- [54] J. Y. Vinet, M. Combescot, and C. Tanguy, Influence of the electron-hole density profile on the reflectivity of laser irradiated silicon, *Solid State Commun.* **51**, 171 (1984).
- [55] Z. Q. Li, V. Podzorov, N. Sai, M. C. Martin, M. E. Gershenson, M. Di Ventra, and D. N. Basov, Light Quasiparticles Dominate Electronic Transport in Molecular Crystal Field-Effect Transistors, *Phys. Rev. Lett.* **99**, 016403 (2007).
- [56] A. Yamamoto, Y. Murata, C. Mitsui, H. Ishii, M. Yamagishi, M. Yano, H. Sato, A. Yamano, J. Takeya, and T. Okamoto, Zigzag-elongated fused π -electronic core: A molecular design strategy to maximize charge-carrier mobility, *Adv. Sci.* **5**, 1700317 (2018).
- [57] S. Uji, J. S. Brooks, M. Chaparala, S. Takasaki, J. Yamada, and H. Anzai, Rapid oscillation and Fermi-surface reconstruction due to spin-density-wave formation in the organic conductor (TMTSF)₂PF₆, *Phys. Rev. B* **55**, 12446 (1997).
- [58] S. Uji, J. S. Brooks, S. Takasaki, J. Yamada, and H. Anzai, Origin of rapid oscillation in the metallic phase for the organic conductor (TMTSF)₂ClO₄, *Solid State Commun.* **103**, 387 (1997).
- [59] See Supplemental Material at <http://link.aps.org/supplemental/10.1103/PhysRevB.107.085147> for details of the simulations of the reflectivity change spectra using the Drude model and the time characteristic of carrier density assuming the Auger recombination processes. See also Refs. [5,14,60,61].
- [60] M. Segawa, A. Takahashi, H. Gomi, and M. Aihara, Auger recombination of photogenerated charges in one-dimensional Mott insulators, *J. Phys. Soc. Jpn.* **80**, 084721 (2011).
- [61] H. Uemura, H. Matsuzaki, Y. Takahashi, T. Hasegawa, and H. Okamoto, Ultrafast charge dynamics in one-dimensional organic Mott insulators, *J. Phys. Soc. Jpn.* **77**, 113714 (2008).
- [62] M. Ogata and H. Shiba, Bethe-ansatz wave function, momentum distribution, and spin correlation in the one-dimensional strongly correlated Hubbard model, *Phys. Rev. B* **41**, 2326 (1990).
- [63] H. Eskes and A. M. Oleś, Two Hubbard Bands: Weight Transfer in Optical and One-Particle Spectra, *Phys. Rev. Lett.* **73**, 1279 (1994).
- [64] W. Stephan and P. Horsch, Optical properties of one- and two-dimensional Hubbard and t - J models, *Phys. Rev. B* **42**, 8736 (1990).
- [65] J. Wagner, W. Hanke, and D. J. Scalapino, Optical, magnetic, and single-particle excitations in the multiband Hubbard model for cuprate superconductors, *Phys. Rev. B* **43**, 10517 (1991).
- [66] E. Dagotto, A. Moreo, F. Ortolani, D. Poilblanc, and J. Riera, Static and dynamical properties of doped Hubbard clusters, *Phys. Rev. B* **45**, 10741 (1992).
- [67] Z. Lenarčič, M. Eckstein, and P. Prelovšek, Exciton recombination in one-dimensional organic Mott insulators, *Phys. Rev. B* **92**, 201104(R) (2015).
- [68] Y. Okimoto, H. Matsuzaki, Y. Tomioka, I. Kezsmarki, T. Ogasawara, M. Matsubara, H. Okamoto, and Y. Tokura, Ultrafast photoinduced formation of metallic state in a perovskite-type manganite with short range charge and orbital order, *J. Phys. Soc. Jpn.* **76**, 043702 (2007).
- [69] M. Dumm, D. Faltermeier, N. Drichko, M. Dressel, C. Mézière, and P. Batail, Bandwidth-controlled Mott transition in κ -(BEDT-TTF)₂Cu[N(CN)₂]Br_xCl_{1-x}: Optical studies of correlated carriers, *Phys. Rev. B* **79**, 195106 (2009).
- [70] T. Hasegawa, T. Mochida, R. Kondo, S. Kagoshima, Y. Iwasa, T. Akutagawa, T. Nakamura, and G. Saito, Mixed-stack organic charge-transfer complexes with intercolumnar networks, *Phys. Rev. B* **62**, 10059 (2000).
- [71] C. Kübler, H. Ehrke, R. Huber, R. Lopez, A. Halabica, R. F. Haglund, Jr., and A. Leitenstorfer, Coherent Structural Dynamics and Electronic Correlations during an Ultrafast Insulator-to-Metal Phase Transition in VO₂, *Phys. Rev. Lett.* **99**, 116401 (2007).
- [72] L. Chen, Y. Cui, H. Luo, and Y. Gao, Atomic and electronic structures of charge-doping VO₂: First-principles calculations, *RSC Adv.* **10**, 18543 (2020).
- [73] A. Cavalleri, T. Dekorsy, H. H. W. Chong, J. C. Kieffer, and R. W. Schoenlein, Evidence for a structurally-driven insulator-to-metal transition in VO₂: A view from the ultrafast timescale, *Phys. Rev. B* **70**, 161102 (2004).